Nanotextured Surface on Flexographic Printed ZnO Thin Films for Low Cost Non-Faradaic Biosensors

Abdulaziz K. Assaifan, [†,‡] *Jonathan S. Lloyd,* [†,‡] *Siamak Samavat,* [†] *Davide Deganello ,* [ℓ] *Richard J. Stanton* [§] *and Kar Seng Teng* [*,†]

†College of Engineering, Swansea University, Bay Campus, Fabian Way, Crymlyn Burrows, Swansea, SA1 8EN, United Kingdom

[ℓ] Welsh Centre for Printing and Coating, College of Engineering, Swansea University, Bay Campus, Fabian Way, Crymlyn Burrows, Swansea, SA1 8EN, United Kingdom

§Institute of Infection & Immunity, School of Medicine, Cardiff University, Henry Wellcome Building, Heath Park, Cardiff, CF14 4XN, United Kingdom

KEYWORDS

flexographic printing, metal oxide, nanotexture, non-faradaic, biosensor

ABSTRACT

In this work, the formation of a nanotextured surface is reported on flexographic printed zinc oxide thin films which provide an excellent platform for low-cost, highly sensitive biosensing applications. The ability to produce nanotextured surfaces using a high throughput, roll-to-roll production method directly from precursor ink without any complicated processes is commercially attractive for biosensors that are suitable for large scale screening of diseases at low cost. The zinc oxide thin film was formed by printing a zinc acetate precursor ink solution and annealing at 300°C. An intricate nanotexturing of the film surface was achieved through 150°C drying process between multiple prints. These surface nanostructures were found to be in the range of 100 to 700 nm in length with a width of 58 ± 18 nm and a height of between 20 and 60 nm. Such structures significantly increase the surface area to volume ratio of the biosensing material which is essential to high sensitivity detection of diseases. Non-faradaic electrochemical impedance spectroscopy measurements were carried out to detect the pp65-antigen of the human cytomegalovirus using the printed device, which has a low limit of detection of 5 pg/ml.

Introduction

Metal oxide semiconductors such as indium tin oxide, zinc oxide (ZnO) and tungsten oxide, can be found in a wide range of applications due to their many advantageous material properties. [1-3] For example, ZnO has been extensively researched for light emitting diodes, solar cells and biosensors, [4-8] among many other applications. The use of metal oxide semiconductors in sensing applications has been successful because they benefit from being relatively inexpensive and robust as well as having quick response times and high sensitivity when compared with other sensing materials.[9] These properties make them useful in a variety of sensing applications such as environmental, chemical and biological sensing.[10-12] Metal oxide nanostructures can further improve the performance of devices as they exhibit large surface area to volume ratio, good electron mobility and biocompatibility.[13] Most ZnO thin films have been deposited onto surfaces using techniques such as chemical vapour deposition, physical vapour deposition and molecular beam epitaxy. [14-16] Surface nanostructures have been developed using techniques such as electron beam lithography, nanoimprint lithography and scanning probe lithography etc. However, these techniques are expensive, time consuming and require complex processing steps, hence they are not ideal for low-cost mass production of highly sensitive biosensors that can be potentially used for large scale screening of diseases. In any screening programs, cost of the device is one of the major key factors to be considered. Therefore, the use of low-cost, high yield manufacturing techniques for the fabrication of ZnO nanostructured biosensors are highly desirable. The use of methods such as flexographic printing of nanostructures onto substrates would significantly reduce the cost and improve the viability of mass production of ZnO devices. Flexographic printing has been previously reported by the authors for selective patterning of seed layers for the growth of ZnO nanowires.[17] The technique

has also been more recently used for the production of thin film transistors with the formation of In_2O_3 layers.[18] In this work, the direct formation of intricate nanotextured surface on flexographic printed ZnO thin films is reported for the first time and demonstrated for biosensing application. These nanoscopic structures were formed without undergoing any complicated post-treatment and are ideal for use as biosensing platform. The device consisting of silver (Ag) electrodes and ZnO thin film was fabricated on organic substrates using the flexographic printing technique, which would simplify the production process and significantly reduce the cost of devices.

Here a precursor ink was deposited through the use of flexographic printing to provide a ZnO thin film onto which bio-receptors can be bound for use as biosensor. The printing of these films is studied with an increasing number of printed ZnO layers. Studies were carried out to investigate the morphology of the printed surface and the structure of the polycrystalline layer. The device was subsequently functionalized with anti-pp65 antibodies and used in non-faradaic electrochemical impedance spectroscopy (EIS) for the rapid detection of human cytomegalovirus (HCMV). The detection of the pp65 HCMV protein was carried out as an example of the device sensing capabilities. Changing the functionalized antibody would allow the detection of other biomarkers for the detection of a wide variety of other diseases. EIS biosensors have been widely investigated for the direct (i.e. label-free), rapid detection of antigens due to its extremely high surface sensitivity. This high surface sensitivity allows the detection of disease biomarkers which can be captured by attached bio-receptors at the surface of the sensor.[19] This is a major motivation towards the use of EIS as most other techniques require their target biomarker to be attached with a label for detection. The pp65 antigen that is detected here, is the most abundant tegument protein within extracellular virus particles of HCMV.[20] HCMV is a wide spread

pathogen that infects the majority of people worldwide by early adulthood.[21] 50% to 85% of the world's population are infected by HCMV by the age of 40.[22] HCMV can cause mortality in individuals with weakened immune systems such as AIDS and organ transplant patients.[23] It is also of significant concern if a woman is infected while pregnant, since the virus can spread to the unborn baby. This affects one to two babies in every two hundred and can result in permanent disabilities, such as mental retardation, blindness, deafness or even fatality to the babies.[24] Early detection, within a month of birth, can lead to early treatment and potentially prevention or reduction of complications in later life.[25] Since a large percentage of congenitally infected babies are not diagnosed at birth, fast, reliable and low cost devices suitable for screening would provide significant patient benefit. Current clinical techniques such as ELISA, virus isolation culture and RT-PCR have several disadvantages. These techniques are expensive, time consuming and require highly trained lab specialists. Others have reported HCMV detection via electrochemical stripping analysis of glycoprotein B, one of the most dominant proteins of HCMV.[26] Quartz crystal microbalance technology [27] and electrochemical detection using an ultramicroelectrode have also been reported. [28] However these technologies lack the scalability in production. The use of biosensors such as those based on EIS can minimize the time and cost of testing, due to their ease of use. [29] The low cost, mass producible, sensitive and accurate point of care diagnostic technology for HCMV being developed here tackles the problems with current methods to enable large scale screening of newborn babies.

1. Experimental Section

1.1 Flexographic Printing of Electrodes and ZnO layer

Prior to printing, polyimide (PI) substrates (Lohmann Adhesive Tape Systems, Milton Keynes, UK) with size of 5 cm x 30 cm were wiped clean with acetone and sonicated for 10 mins in acetone followed by isopropanol, and then blown dry with nitrogen. After vigorous mixing, Ag ink (Novacentrix, Austin, Texas) was printed onto the PI substrate using an IGT Reprotest Printability Tester F1 Flexographic printer (Schematic diagram shown in Supporting Information Figure S1). The working principle of the flexographic printer is detailed in previous work by the authors.[17] Briefly, ink is placed onto an anilox roller that transfers a controlled volume of ink to the printing plate (a photopolymer with desired image in relief) which subsequently prints the desired pattern onto the substrate. The technique is ideal for high volume mass production as it provides continuous roll-to-roll printing.

After printing the Ag electrodes the samples were dried at 150^{o}C for 5 mins in an oven. The Ag ink was sintered by further annealing the substrate to 350°C for 20 mins on a hotplate. The zinc acetate ($Zn(O_2CCH_3)_2$) ink solution was prepared by dissolving 0.1 M zinc acetate in 10 ml deionised water and subsequently adding 40 ml isopropanol to improve wetting of the ink on the substrate. Before printing the zinc acetate ink, the printed Ag substrates were sonicated in ethanol for 10 mins to reduce the surface oxides and remove any physically adsorbed particles and contaminants that can contribute to unwanted electrochemical effects.[30] The zinc acetate ink was then printed over the top of the electrodes using the optimized printing parameters. To investigate the coverage of ZnO on the printed Ag electrodes, multiple zinc acetate layers (1, 3 and 6) were printed. Printed zinc acetate samples were dried immediately at 150^{o}C for

approximately 30s to dry the ink before printing the next layer. After printing the layers, the sample was placed in an oven at 300^{o}C for 30 mins to allow conversion of zinc acetate to ZnO. This printing process led to a nanotextured ZnO surface ideal for high loading of bio-receptors. The optimal printing parameters for printing the Ag ink and zinc acetate ink using the F1 printer, are summarized in Table 1.

Table 1. Optimised flexographic printing parameters for Ag and zinc acetate inks.

Parameter	Ag Ink	Zinc Acetate Ink
Anilox roller volume [cm^3 m^{-2}]	8	12
Anilox force[a)] [N]	50	125
Printing force[a)] [N]	50	150
Printing speed [m s^{-1}]	0.8	0.2

[a)] See Figure S1 in Supporting Information for illustration of force directions

1.2 Characterization

A range of techniques were employed to characterize the printed layer and the performance of the fabricated biosensors. High resolution images of the resultant ZnO layer were obtained using a Hitachi S-4800 SEM and a JPK Instruments atomic force microscope (AFM) used in AC mode with appropriate tapping mode RTESP AFM probes (Bruker, USA). X-ray photoelectron spectroscopy (XPS) analysis was carried out at room temperature using the Kratos Axis Supra system equipped with a monochromatic Al Kα source with energy of 1486.6 eV. For crystallinity analysis a Bruker D8 Discover X-ray diffraction (XRD) system, equipped with a Cu Kα (0.15418 nm wavelength) x-ray source and a Lynxeye detector, was used. To evaluate the

suitability of the annealing temperature a Perkin Elmer STA6000 simultaneous thermal analyser was used. The STA6000 used here was equipped with a Perkin Elmer TL9000 transfer line to a Perkin Elmer FTIR spectrum 100 for Fourier transform infrared (FTIR) analysis of the exhaust gasses. This allowed identification of compounds released from the sample during the thermal analysis. The biosensors were studied through the use of non-faradaic EIS, performed using a Gamry reference 600 potentiostat.

1.3 Bio-Functionalization

A schematic of the printed device is shown in Figure 1(a) and an illustration of the functionalization steps of the biosensor is shown in Figure 1(b-d). The silane groups of (3-Aminopropyl)triethoxysilane APTES binds covalently to the native hydroxyl groups of the ZnO layer (Figure 1(b)). Subsequently, the aldehyde groups of the glutaraldehyde covalently bind to the exposed amine groups of the APTES layer (Figure 1(c)). The amine groups of the antibody then bind to the exposed aldehyde groups of the glutaraldehyde (Figure 1(d)).

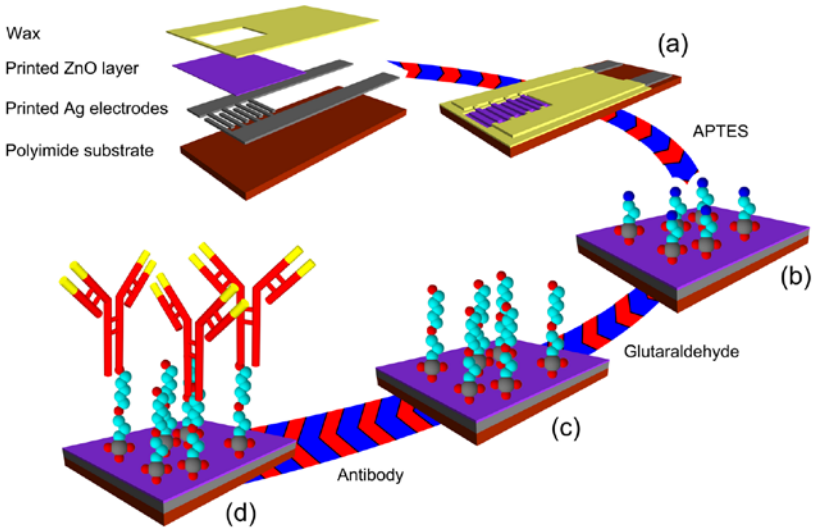

Figure 1. Schematic of the fabrication and functionalization steps of the biosensor.

The ZnO thin film, with 6 prints, was firstly treated with 2% APTES in ethanol at 70^{o}C in a sealed container for 10 minutes. It was then washed twice in ethanol to remove loosely physisorbed APTES and blow dried with N_2. Subsequently, the APTES coated surface was annealed at 120^{o}C for 20 mins under continuous N_2 flow. It has been previously reported that annealing the APTES layer densifies the layer due to promotion of condensation reactions between the side arms of the APTES molecules.[31] Paraffin wax was then used to define the sensing window (5 mm x 8 mm). The sensing window was treated with 2.5% glutaraldehyde in phosphate buffered saline (PBS) for 1 hour and then washed with PBS and dried with N_2. This was followed by an incubation of 50 µl of 10 µg mL^{-1} anti-pp65 antibody (Virusys-Corporation, Maryland, United States) in deionised water for one hour. The sensing window was subsequently washed with deionised water. The sensing window was then exposed to 50 µl of 50 mM ethanolamine (pH 8.5) for 15 mins to deactivate the unreacted aldehyde groups of the glutaraldehyde and was washed as previous.[32] The slightly elevated pH of the ethanolamine solution also aids in removing unbound antibody from the surface. Finally, 100 µl of 5% bovine serum albumin (BSA) was incubated onto the sensing window for 30 mins and washed as previous. The BSA blocks sites where proteins could non-specifically absorb onto the sensor surface, improving the selectivity of the sensor.

1.4 EIS Sensor Testing

EIS sensors can be operated in two different detection modes, namely faradaic and non-faradaic. The use of faradaic EIS offers low detection limits. However, it requires the use of redox probes to be introduced to the sample of interest, hence requiring a sample preparation step. The use of non-faradaic EIS eliminates the need for this sample preparation step as no

redox probe is required and the capacitance is measured instead of the charge transfer resistance. Hence non-faradaic sensors are sometimes referred to as capacitive biosensors. Non-faradaic sensors therefore provide a pathway towards simple to use point-of-care diagnostic devices without the need for sample preparation. To the author's knowledge, this is the first time that direct detection of HCMV proteins has been performed with non-faradaic EIS. For EIS measurements, AC signals of different frequencies are applied between the two electrodes while the voltage and current is monitored. This allows the frequency dependent impedance to be measured. For non-faradaic measurements, the attachment of molecules to the surface displaces water molecules, reducing the dielectric constant at the surface, hence reducing the surface capacitance.[33] To perform the EIS measurements the devices were connected to the potentiostat and 100 µl of PBS was added to the sensing window. EIS measurements were performed over a frequency range of 50 mHz to 1 kHz with an applied AC potential of 10 mV until a stable baseline reading was achieved. The PBS solution was then replaced with 100 µl pp65-antigen (Miltenyl Biotec Ltd, Surrey, UK) in PBS, incubated for 15 mins and then a further EIS measurement was carried out. This procedure was repeated for different concentrations of pp65-antigen between 0.385 ng mL^{-1} and 38.5 µg mL^{-1} with EIS measurements performed after each incubation period. Similar measurement were carried out with just PBS (as negative samples, i.e. without the addition of pp65-antigen) to determine the response of the biosensor to negative samples. Changes in phase and capacitance were normalized to the baseline of the biosensor for both positive and negative sample tests.

To assess the selectivity of the biosensor, tests were performed on a mixture of other proteins. The biosensors were incubated for 15 mins with a mixture of gB-antigen (AbD serotec, Kidlington, UK), collagen (Jellagen, Pembroke Dock, UK), BSA and pp65-antigen, each having

a concentration of 40 µg mL^{-1}. The result was compared with biosensors incubated with the above mixture at the same concentration but without pp65-antigen. In both tests, the biosensors were exposed to a range of proteins but only one set had the pp65 protein. Such tests mimic clinical samples which contain a mixture of many proteins.

2. Results and Discussion

2.1 Nanotextured Surface at Printed ZnO Layer

Ag interdigitated electrodes were printed onto PI substrate as described in the methods section and subsequently overprinted with 1, 3 or 6 layers of zinc acetate ink. After annealing, the resultant ZnO layers were characterized. To fabricate a device from a printed precursor ink it is important to ensure that conversion of the zinc acetate to ZnO is achieved. It has been well reported that thermal decomposition of zinc acetate will form ZnO. [17, 34, 35] Here a temperature of 300°C, which is 50°C less than the glass transition temperature of the PI substrate, is desirable. The thermogravimetric analysis (TGA) data in Figure 2(a) shows the percentage weight loss of dried zinc acetate ink (red, dotted curve), the temperature profile used (thick, black, solid curve) and the measured sample temperature (black, dashed line). The temperature profile consisted of raising the temperature of the samples to 300°C with a high ramp rate of 100°C min^{-1} from an initial temperature of 30°C. The sample was then held in an isotherm of 300°C for 30 mins before being ramped up to 450°C at 20°C min^{-1} and held for 4 mins.

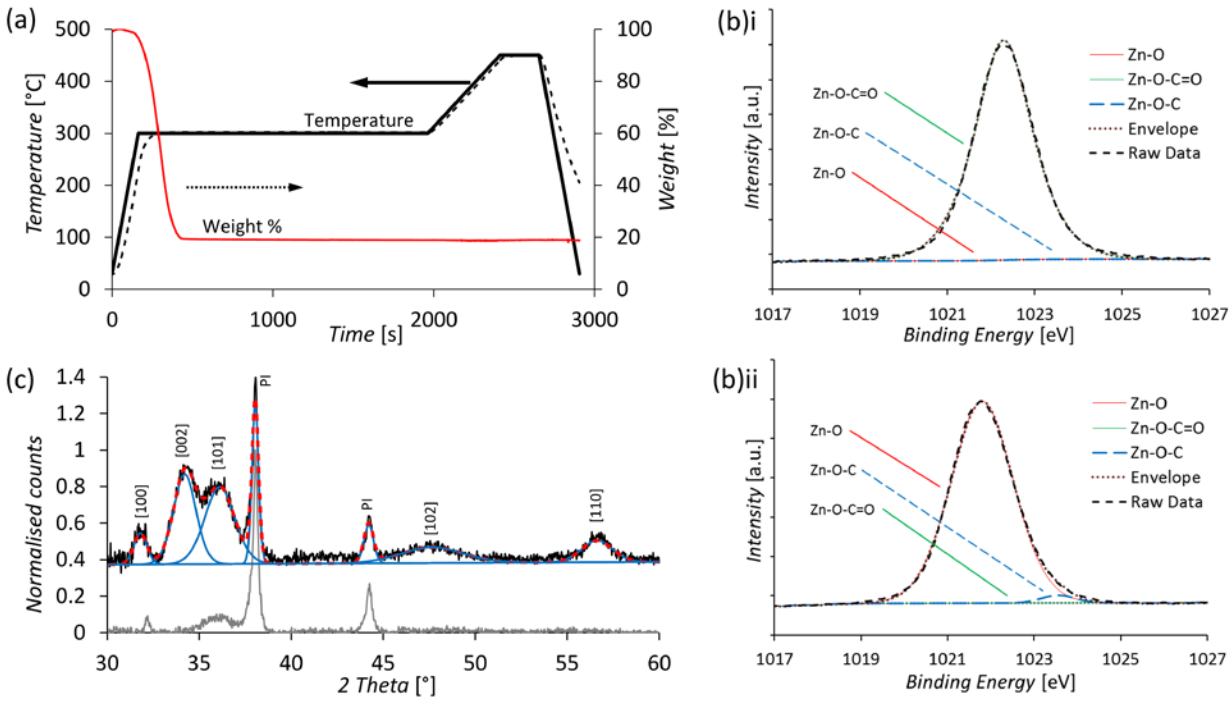

Figure 2. Thermal decomposition analysis of zinc acetate ink to ZnO (a) TGA weight loss analysis (red dotted line), temperature profile (solid black line) and measured sample temperature (black dashed line), (b) XPS Zn 2p3/2 peak position (i) before and (ii) after annealing and (c) XRD spectra with and without ZnO layer and with curve fitting.

It can be seen from the profile shown in Figure 2(a), that after around 200 s the mass starts to drop as the thermal decomposition takes place. After 440 s, which is 280 s after the start of the isotherm, the weight percentage is 20%. During the rest of the isotherm a further 0.5% drop in weight percentage was observed. The final section of the cycle which brought the sample temperature up to 450°C revealed no further loss in mass. This indicates that after 30 mins at 300°C no further decomposition occurs and after just 440 s 99.3% of the mass loss had occurred. This indicates that the annealing time could be reduced to well below 30 mins. Samples used in

this work were annealed at 300°C for 30 mins which allowed decomposition of the zinc acetate ink.

FTIR analysis of the exhaust gasses from the TGA chamber (example shown in the Supporting Information Figure S2) confirms the loss of compounds containing C-O, C=O, O-H and C-H bonds. These bonds are associated with the acetate groups lost during the thermal decomposition. These peaks are large in the FTIR data collected at 240 s which corresponds to the time of greatest rate of mass loss from the sample. These peaks are only present in the FTIR data between around 100 s to 450 s which corresponds to the mass loss period.

XPS analysis of the printed samples, before and after annealing at 300°C, further confirms the conversion of zinc acetate ink to ZnO. Figure 2(b)i and (b)ii show the high resolution XPS scans of the Zn $2p_{3/2}$ peak for two samples, before and after annealing, respectively. The Zn $2p_{3/2}$ peaks have been fitted with two main curves at 1021.8 eV and 1022.4 eV corresponding to Zn-O bonding of ZnO and Zn-O-C=O bonding of zinc acetate respectively.[36] For a sample of drop cast zinc acetate ink, dried at room temperature without any annealing, the single curve at 1022.4 eV, which corresponds to Zn-O-C=O bonding of zinc acetate, dominates the peak. The data shows no component associated with ZnO which would be located at 1021.8 eV. In contrast, after the annealing process, the Zn $2p_{3/2}$ peak has shifted towards lower binding energy with a good fit from the Zn-O curve and no contribution from the Zn-O-C=O curve. However, a small secondary component at 1023.6 eV is present. This second curve at 1023.6 eV has been assigned to adventitious carbon contamination on the surface of the ZnO (i.e. Zn-O-C) since the samples were annealed in air. The main curve, which corresponds to the Zn-O bonding of ZnO, makes up 98% of the composition. The carbon (C 1s) and oxygen (O 1s) peaks from the XPS have been curve fitted and are shown in the Supporting Information (Figure S3). Upon annealing at 300°C,

the intensity of O-C=O and C=O peaks, associated with the acetate groups in the C 1s and O 1s peaks respectively, were significantly reduced which indicated the loss of the acetate groups. This is in good agreement with the FTIR analysis of the exhaust gasses during the TGA measurements. XRD analysis of a 6 print sample is shown in Figure 2(c). The spectra were taken with grazing incidence to reduce the influence of the bulk substrate on the diffractogram, therefore enhancing the signal from the surface where the layer of interest resides. Some peaks from the underlying substrate are still visible and can be seen in both the bare substrate scan (grey line) and the ZnO printed substrate scan (black line). The extra peaks observed in the ZnO printed substrate scan, located at 31.7°, 34.2°, 36.1°, 47.5° and 56.7° are associated with the hexagonal wurtzite phase of ZnO and assigned as [100], [002], [101], [102] and [110] crystal orientations respectively.[36-38] These peak positions match closely with ZnO on the crystallography open database (COD 9004178). This combination of TGA, XPS and XRD analysis verified that a conversion of the zinc acetate to ZnO has been achieved at 300°C. This temperature is well below the glass transition temperature of the PI substrate, hence avoiding damage to the substrate and yet, as demonstrated, high enough to ensure conversion to ZnO.

The peak width from XRD is inversely proportional to domain size and therefore the observed broad peaks in this diffractogram indicate that the layer is made up of small domains. The size of the domains can be approximated using the Scherrer model shown in Equation 1.

$$t = \frac{K\lambda}{\beta Cos\theta} \quad (1)$$

where t is the domain size, K is the shape factor, λ is the x-ray wavelength, β is the peak broadening and θ is the Bragg angle. For the estimation of the particle size, a shape factor of 0.9 was used to represent domains almost spherical in shape (the particles can be seen in the high magnification SEM images shown in Figure S4 of the Supporting Information). The Bragg angle

and full width half maximum (FWHM) of the peaks were calculated by curve fitting of the XRD peaks with Gaussian curves. The fitted curves along with an envelope created during the fitting process are shown on the XRD plot in Figure 2(c) and represented by blue dotted and red dashed curves respectively. A summary of the Bragg angles and FWHM for each of the ZnO peaks is shown in Table 2.

Table 2. Bragg angles and FWHM's of XRD peaks from Gaussian curve fits and estimated particle size using the Scherrer model.

Bragg Angle (2θ) [°]	Peak Identification	FWHM [°]	Predicted Domain Size [nm]
31.8	[100]	0.80	11.7
34.2	[002]	1.47	6.5
36.1	[101]	1.94	5.1
47.6	[102]	2.80	4.2
56.7	[110]	1.74	8.3
		Average	7.2
		Standard Deviation	2.7

The peaks generated by the substrate have not been included. From this data, domain sizes have been calculated for each peak and the average of the calculated domain sizes is 7.2 ± 2.7 nm.

The uniformity and morphology of the resultant ZnO layer was studied. XPS, which is a surface-sensitive analytical technique, was used to evaluate the coverage of ZnO over the Ag surface by observing the reduction of the Ag peak as the number of printed zinc acetate layers

increased. Wide area (i.e. scan area of 300 μm by 800 μm) XPS spectra of ZnO/Ag samples with different printed layers of zinc acetate ink after annealing to form ZnO layers are presented in Figure 3(a).

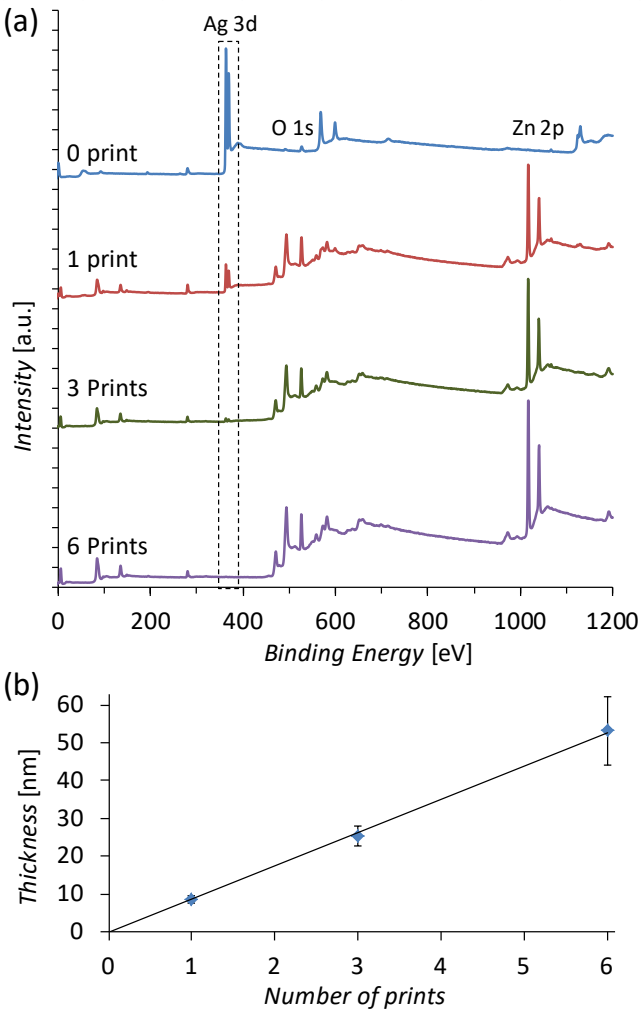

Figure 3. Analysis of the surface coverage and thickness of the ZnO layer (a) XPS survey scans with Ag 3d peak highlighted and (b) AFM measurements of ZnO film thickness.

The peaks at 368eV, 531eV and 1022eV correspond to Ag 3d, O 1s and Zn 2p respectively. It can be seen that the Zn 2p and O 1s peaks are clearly present in the three samples with ZnO layers (e.g. samples with 1, 3 and 6 printed zinc acetate layers). The Zn 2p peak is not present for

the sample without zinc acetate printing (i.e. 0 print) since there is no Zn present. The O 1s peak is much smaller for the sample with no ZnO layer but still observable, this is due to native surface oxides on the Ag electrode. With more printed layers it can be seen that the Ag 3d peak (highlighted with dashed box) diminishes. With 6 prints no detectable Ag was observed. Ag exposure on the samples with fewer prints is attributed to non-uniformity in the printed layer due to the high surface roughness of the underlying Ag electrode. This roughness is on the scale of a few hundreds of nm and can cause the ink to pool in the lower regions, hence exposing peaks of Ag. Therefore samples with 6 prints were used for the device to ensure that the ZnO has a complete coverage on the Ag electrodes. Also, the exposure of the Ag during biosensing tests could be detrimental due to the reactivity of Ag. AFM measurements were carried out on a step edge at the PI/ZnO interface to measure the thickness of the ZnO layers. The results are shown in Figure 3(b) where it can be seen that the deposition is roughly linear, with each printed layer adding approximately 8.8 nm to the total thickness of the printed ZnO layer.

The printed zinc acetate layer followed by thermal decomposition has resulted in a polycrystalline ZnO film. SEM images shown in Figure 4(a)i-iv illustrate that the resultant ZnO layer, after annealing, is made up of many interconnected ZnO nanoparticles with size of a few nanometers. The submicron grains observed in the SEM images are the underlying printed Ag electrode. The SEM images also show increased density of nanoparticles on the Ag surface with increasing number of prints. For a single print, as shown in Figure 4(a)ii, it can be seen that the density of the nanoparticles is non-uniform with a lower density in the higher regions of Ag and a higher density in the troughs. This non-uniformity of the ZnO nanoparticles on the rough Ag electrode surface agrees with the XPS results. The exposure of Ag shown by XPS, for samples with fewer prints, is most likely caused by the pooling of ink in these lower regions. This causes

Ag at the higher regions to become exposed, which was then detected using the XPS. SEM images of printed regions on the PI substrate show a more uniform coverage due to the smoother underlying surface (images shown in Supporting Information Figure S5). For samples with 6 prints, it can be seen from Figure 4(a)iv that intricate nanoscale features are formed on the surface of the sample. These surface features are forming over the printed areas, such as on Ag electrodes and PI substrate, and are made up of aggregated ZnO nanoparticles.

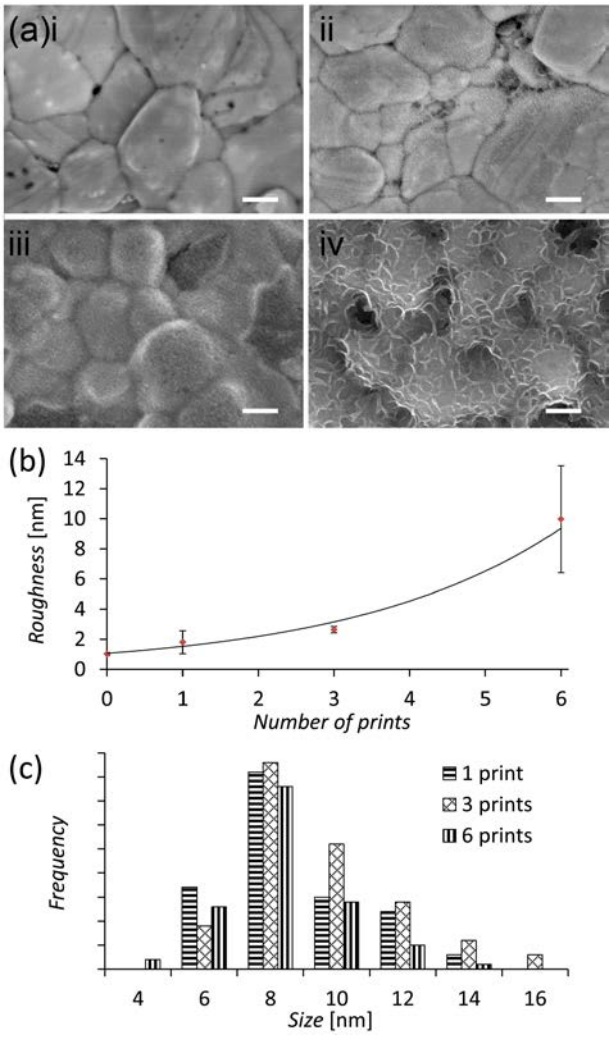

Figure 4. Morphological analysis of resultant ZnO layer using (a) SEM imaging for (i) bare Ag, (ii) 1 printed layer, (iii) 3 prints and (iv) 6 prints (scale bar is 300 nm), (b) AFM roughness analysis (2 x 2 μm scans) and (c) Particle size analysis from high magnification SEM images.

AFM analysis of the printed layers was carried out in areas of PI rather than Ag so the roughness measurement is of the ZnO layer and not dominated by the Ag roughness. This analysis shows topographical changes with number of prints. Roughness measurements were taken on 0, 1, 3, and 6 print samples and were averaged over 4 different scan areas of 2 μm x 2 μm. A graph of the results of the roughness analysis is shown in Figure 4(b) where it can be seen

that the roughness drastically increases with increased prints (for 3D representations of typical AFM images for 1, 3 and 6 printed layers see Supporting Information Figure S6). Figure 4(c) shows a particle size distribution plot carried out on high magnification SEM images. The average particle size and standard deviation for 1, 3 and 6 print samples was determined to be 7.8 ± 2.0 nm, 8.5 ± 2.2 nm and 7.2 ± 1.8 nm respectively. The similarity between these sizes indicates that the particle size is independent of the final layer thickness. It is anticipated that the particle size is more dependent on the annealing process than the number of prints.[39] The particle size found here correlates well with the average size estimated from the XRD peak widths. This suggests that the majority of the nanoparticles, as seen in the SEM are single crystalline domains of ZnO. Furthermore, the increasing roughness observed in the AFM analysis is caused by particle grouping and stacking rather than particle size changes. It can be seen from the SEM images (more apparent on the 6 print samples in Figure 4(a)iv) that the aggregation of these ZnO nanoparticles resulted in a nanotextured surface and therefore increases the surface roughness of the ZnO samples. These nanotextured surface features have been measured from multiple SEM images to be in the range of 100 to 700 nm in length and a width of 58 ± 18 nm.

AFM imaging of the nanotextured surface of the ZnO layer on the Ag electrode reveals a similar surface morphology as seen in the SEM images. The height of the nanotextured features was measured from the AFM images. The height was found to vary between the high and low regions of the submicron grains of Ag, again attributed to the pooling of ink in the low regions and also the low regions experience reduced contact with the printing plate. The height of the features were measured from cross sections taken from AFM images to be 26 ± 7 nm and 53 ± 11 nm in the high and low regions of Ag respectively. Examples of typical AFM cross sections

from a high and low region at the Ag grains are shown in Figure 5, represented by a dashed red line and a solid blue line respectively.

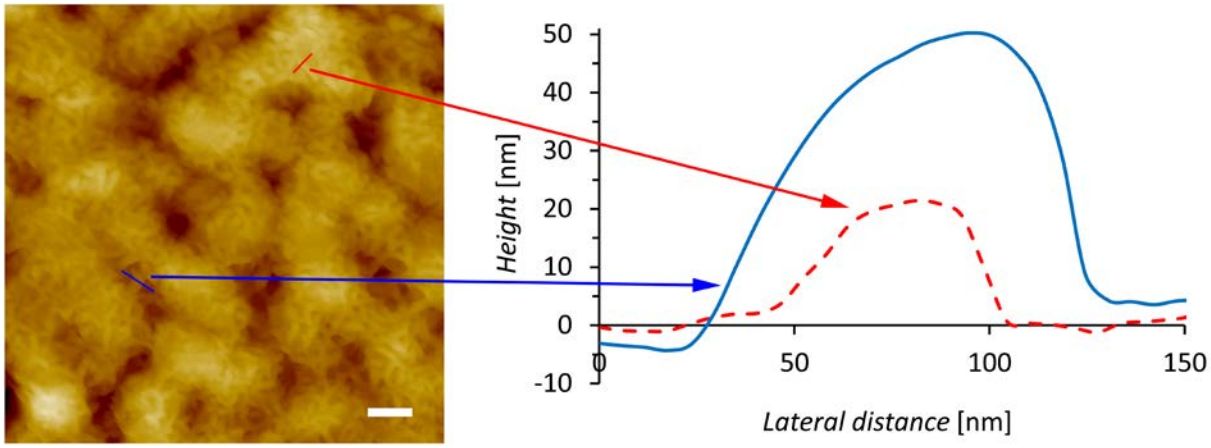

Figure 5. AFM surface morphology analysis of ZnO structures on Ag surface with a 3 x 3 µm AFM scan (300nm scale bar) and indicated line profiles showing the height of the structures on the top of the Ag particles (red dashed line) and in the low regions of the Ag surface (blue solid line).

It is thought that the formation of these nanotextured features occurs during the drying phase of the ink between each subsequent print. Surface imperfections beneath the printed layer could act as local pinning points during later stages of the drying process, so that as liquid evaporates these points must be replenished by liquid from the surroundings.[40] The resulting flow would carry zinc acetate precursor towards these areas, creating a high point on the surface after drying. These deposits would encourage seeding at the same point in the subsequent printed layers. In this way, the phenomenon will increase the size of these nanotextured features with further print and dry cycles. Due to the high content of isopropanol in the ink it is anticipated that the vast majority of the particle formation will occur after the printed liquid layer has dried. SEM

imaging of drop cast zinc acetate ink (with no heat treatment) shows no evidence of any particles and a Malvern zeta sizer used to size particles in the ink solution was unable to provide any meaningful data. This leads to the conclusion that the particles are formed by the heating steps and do not already exist in the ink itself. ZnO crystals start to form at temperatures as low as 80°C but higher temperatures tend to provide better crystal structure and higher conversion efficiency.[39] SEM images of samples after printing, which have been exposed to 150°C for 30 s between printed layers, show that particles are starting to form and that the nanoscale features are present (image shown in Supporting Information Figure S7(a)). XPS analysis of printed samples with exposure to the short 150°C drying steps show partial conversion to ZnO. The data, shown in Supporting Information Figure S7(b), indicates approximately 80% of the sample has converted to ZnO. This suggests that particle formation initiates during the 150°C heat treatment between each printed layer.

The nanotextured surface features, most prevalent in the 6 print samples, could prove useful in developing highly sensitive biosensors. Therefore the biosensors reported here are from devices, which have undergone 6 printed layers. These devices were subsequently functionalized and tested for the non-faradaic detection of HCMV.

2.2 Biosensor Performance

To assess the performance of the sensors, biosensing was performed on samples of PBS containing different concentrations of the pp65-antigen (positive samples). Biosensors were tested with successive samples of the pp65-antigen with increasing concentration from 0.385 ng mL^{-1} to 38.5 μg mL^{-1}. They were also tested in the same way with successive samples containing zero antigen concentration (negative samples), which consisted of purely PBS. This combination

of positive and negative sample testing shows that the biosensor is responding to the binding of antigen and not due to unwanted changes to the surface caused by changing the testing solution, washing or the EIS test itself. A decrease in both the measured phase and capacitance was observed after the biosensor was incubated with pp65-antigen. The negative samples showed significantly smaller changes. This indicates that the biosensor is indeed detecting the pp65-antigen. Figure 6(a) and Figure 6(b) show the changes in capacitance and phase at the biosensor with different concentrations of pp65-antigen in PBS and negative samples consisting of only PBS carried out in triplicate. The change in capacitance and phase were measured from the collected EIS data at 50 mHz where the sensors provided the largest response (positive to negative ratio). As can be seen, a decrease in capacitance and phase occurs when the biosensor is incubated with pp65-antigen. It can be seen that the sensor showed a strong response from the capacitance change with less deviation as compared to phase change. The limit of detection (LoD) for the sensors was calculated for both the capacitance and phase graphs giving 5 pg ml^{-1} and 60 pg ml^{-1} respectively. This further indicates that the capacitance of the sensors should be the preferred measured parameter. The LoD was obtained from the standard formula of $3\sigma/m$ where σ is the standard deviation of the negative samples and m is the sensitivity or slope of the calibration curve. The LoD was therefore obtained by finding the intercept of the calibration curves with $y = 3\sigma$. The sensitivity of the sensors, calculated from the slope of the calibration curve was found to be 0.07 µF/ln(ng/ml) and 0.19°/ln(ng/ml) for capacitance and phase respectively. The use of ln(ng/ml) is due to the logarithmic nature of the sensor response as seen by the concentrations increasing 10 fold on the x axis of the calibration curves. It can be seen from the negatives that the sensors are relatively stable over the test period with only minor changes are observed in the capacitance of the sensor over the duration of a six concentration

test. For diagnostics the sensor would be used for a single test concentration and therefore in a much less time. Sensors were also tested after three days of storage in a BSA solution. These sensors showed signals within the standard deviation of the sensors tested immediately after fabrication. An example of an original Bode plot for a sensor tested in positive samples, over the full test frequency range, is shown in the Supporting Information (Figure S8(a)). This plot shows that the impedance is steady while the phase shifts as the device is incubated in increasing pp65-antigen concentrations. Figure S8(b) in the Supporting Information shows the capacitance of the device reducing with increasing concentrations of pp65-antigen.

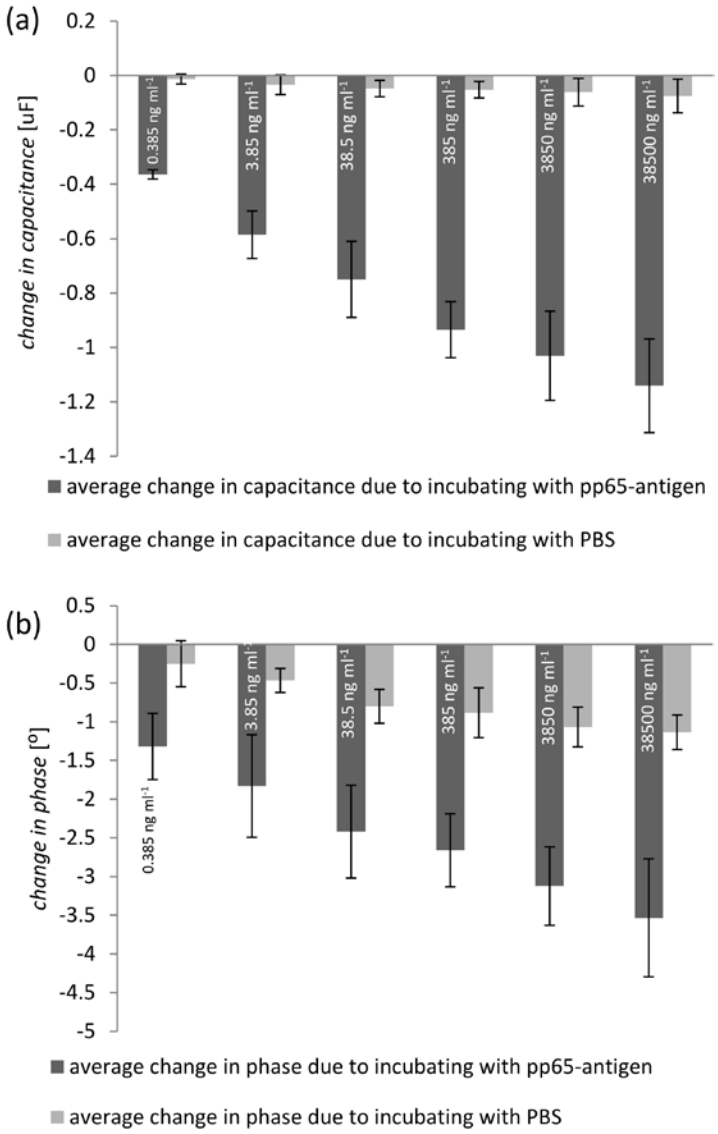

Figure 6. Biosensor response at 50 mHz to increasing concentration of pp65-antigen carried out in triplicate for positive and negative samples (a) change in capacitance and (b) change in phase.

2.3 Selectivity Test

Selectivity of the biosensor to the pp65-antigen was tested against other proteins. Figure 7 shows a change of -2.6±0.4 μF and -1.13±0.04° for capacitance and phase respectively after incubation in a positive sample containing a mixture of gB, collagen, BSA and pp65-antigen tested in triplicate. Figure 7 also shows the change in capacitance and phase due to incubating the biosensor with negative samples of gB, collagen and BSA without pp65-antigen and tested in triplicate to be -0.3±0.2 μF and -0.09±0.19° respectively. This shows that the biosensor is selectively detecting pp65-antigen in a mixture containing other proteins and is not simply detecting any protein non-specifically attaching to the surface of the biosensor.

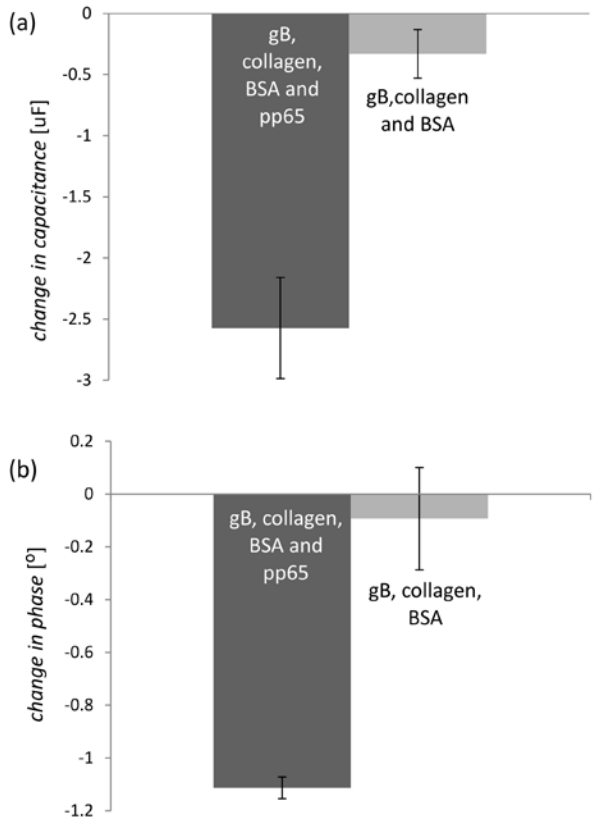

Figure 7. Selectivity test of the biosensor. Sensors were tested in triplicate with pp65 positive and negative samples both containing a mixture of other proteins indicating good selectivity. Data taken from EIS spectra at 50 mHz for both (a) change in capacitance and (b) change in phase.

3. Conclusion

Direct fabrication of immunosensors consisting of ZnO nanotextured surfaces using the roll-to-roll flexographic printing technique was demonstrated. ZnO thin films were produced from printed layers of zinc acetate ink followed by annealing at 300°C to allow thermal decomposition of the precursor to ZnO. An intricate nanotextured surface was formed during the drying process between printed layers. The nanotextured surface is excellent for maximizing surface functionalization, which provides high sensitivity in the detection of biomarkers. Non-faradaic

biosensors fabricated through the printing technique were tested against HCMV pp65-antigen demonstrating a low detection limit of 5 pg ml^{-1} with good selectivity to the antigen among a mixture of other proteins. This facile method of developing nanotextured surfaces would provide a pathway towards low-cost, highly sensitive and mass producible biosensors that are ideal for large-scale screening of diseases.

ASSOCIATED CONTENT

Supporting Information

This material is available free of charge via the Internet at http://pubs.acs.org."

Corresponding Author

*E-mail: k.s.teng@swansea.ac.uk

Author Contributions

The manuscript was written through contributions of all authors. All authors have given approval to the final version of the manuscript. ‡These authors contributed equally.

ACKNOWLEDGMENT

This paper presents independent research funded by the National Institute for Health Research (NIHR) under its Invention for Innovation (i4i) Programme (Grant Reference Number II-LB-0813-20001). The views expressed are those of the author(s) and not necessarily those of the NHS, the NIHR or the Department of Health

REFERENCES

1. Ahammad, A. J. S.; Choi, Y. H.; Koh, K.; Kim, J. H.; Lee, J.-J.; Lee, M., Electrochemical Detection of Cardiac Biomarker Troponin I at Gold Nanoparticle-Modified ITO Electrode by Using Open Circuit Potential. *Int. J. Electrochem. Sci* **2011,** *6* (6), 1906-1916.

2. Chang, C. J.; Hung, S. T.; Lin, C. K.; Chen, C. Y.; Kuo, E. H., Selective Growth of ZnO Nanorods for Gas Sensors Using Ink-Jet Printing and Hydrothermal Processes. *Thin Solid Films* **2010,** *519* (5), 1693-1698.

3. Zheng, H.; Ou, J. Z.; Strano, M. S.; Kaner, R. B.; Mitchell, A.; Kalantar-zadeh, K., Nanostructured Tungsten Oxide - Properties, Synthesis, and Applications. *Adv. Funct. Mater* **2011,** *21* (12), 2175-2196.

4. Kim, K. W.; Choi, N. J.; Kim, K. B.; Kim, M.; Lee, S. N., Growth and Characterization of Nonpolar (10-10) ZnO Transparent Conductive Oxide on Semipolar (11-22) GaN-Based Light-Emitting Diodes. *J. Alloys Compd* **2016,** *666*, 88-92.

5. Bai, Z.; Zhang, Y., Self-Powered UV-Visible Photodetectors Based on ZnO/Cu2O Nanowire/Electrolyte Heterojunctions. *J. Alloys Compd* **2016,** *675*, 325-330.

6. Zhu, P.; Weng, Z.; Li, X.; Liu, X.; Wu, S.; Yeung, K. W. K.; Wang, X.; Cui, Z.; Yang, X.; Chu, P. K., Biomedical Applications of Functionalized ZnO Nanomaterials: from Biosensors to Bioimaging. *Adv. Mater. Interfaces* **2016,** *3* (1), 1-30.

7. Zhao, Z. W.; Chen, X. J.; Tay, B. K.; Chen, J. S.; Han, Z. J.; Khor, K. A., A Novel Amperometric Biosensor Based on ZnO : Co Nanoclusters for Biosensing Glucose. *Biosens. Bioelectron* **2007,** *23* (1), 135-139.

8. Miao, F.; Lu, X.; Tao, B.; Li, R.; Chu, P. K., Glucose Oxidase Immobilization Platform Based on ZnO Nanowires Supported by Silicon Nanowires for Glucose Biosensing. *Microelectron. Eng* **2016,** *149,* 153-158.

9. Fine, G. F.; Cavanagh, L. M.; Afonja, A.; Binions, R., Metal Oxide Semi-Conductor Gas Sensors in Environmental Monitoring. *Sensors* **2010,** *10* (6), 5469-5502.

10. Williams, D. E., Semiconducting Oxides as Gas-Sensitive Resistors. *Sens. Actuators, B* **1999,** *57* (1-3), 1-16.

11. Chen, C. L.; Yang, C. F.; Agarwal, V.; Kim, T.; Sonkusale, S.; Busnaina, A.; Chen, M.; Dokmeci, M. R., DNA-Decorated Carbon-Nanotube-Based Chemical Sensors on Complementary Metal Oxide Semiconductor Circuitry. *Nanotechnology* **2010,** *21* (9) 1-8.

12. Tarlani, A.; Fallah, M.; Lotfi, B.; Khazraei, A.; Golsanamlou, S.; Muzart, J.; Mirza-Aghayan, M., New ZnO Nanostructures as Non-Enzymatic Glucose Biosensors. *Biosens. Bioelectron* **2015,** *67,* 601-607.

13. Yang, P. D.; Yan, H. Q.; Mao, S.; Russo, R.; Johnson, J.; Saykally, R.; Morris, N.; Pham, J.; He, R. R.; Choi, H. J., Controlled Growth of ZnO Nanowires and their Optical Properties. *Adv. Funct. Mater* **2002,** *12* (5), 323-331.

14. Lu, J. G.; Kawaharamura, T.; Nishinaka, H.; Kamada, Y.; Ohshima, T.; Fujita, S., ZnO-Based Thin Films Synthesized by Atmospheric Pressure Mist Chemical Vapor Deposition. *J. Cryst. Growth* **2007,** *299* (1), 1-10.

15. Blackwell, S.; Smith, R.; Kenny, S. D.; Walls, J. M.; Sanz-Navarro, C. F., Modelling the Growth of ZnO Thin Films by PVD Methods and the Effects of Post-Annealing. *J. Phys.: Condens. Matter* **2013,** *25* (13) 1-12.

16. Meng, L.; Zhang, J.; An, J.; Hou, X., Stable P-Type ZnO Thin Films on Sapphire and N-Type 4H-SiC Achieved by Controlling Oxygen Pressure Using Radical-Source Laser Molecular Beam Epitaxy. *Phys. Status Solidi A* **2016,** *213* (1), 72-78.

17. Lloyd, J. S.; Fung, C. M.; Deganello, D.; Wang, R. J.; Maffeis, T. G. G.; Lau, S. P.; Teng, K. S., Flexographic Printing-Assisted Fabrication of ZnO Nanowire Devices. *Nanotechnology* **2013,** *24* (19) 1-7.

18. Leppaniemi, J.; Huttunen, O.-H.; Majumdar, H.; Alastalo, A., Flexography-Printed In2O3 Semiconductor Layers for High-Mobility Thin-Film Transistors on Flexible Plastic Substrate. *Adv. Mater* **2015,** *27* (44), 7168-7175.

19. Bahadir, E. B.; Sezginturk, M. K., A Review on Impedimetric Biosensors. *Artif. Cells, Nanomed., Biotechnol* **2016,** *44* (1), 248-262.

20. Chevillotte, M.; Landwehr, S.; Linta, L.; Frascaroli, G.; Luske, A.; Buser, C.; Mertens, T.; von Einem, J., Major Tegument Protein pp65 of Human Cytomegalovirus Is Required for the Incorporation of pUL69 and pUL97 into the Virus Particle and for Viral Growth in Macrophages. *J. Virol* **2009,** *83* (6), 2480-2490.

21. Tomtishen, J. P., III, Human Cytomegalovirus Tegument Proteins (pp65, pp71, pp150, pp28). *Virol. J* **2012,** *9-22*.

22. Selinsky, C.; Luke, C.; Wloch, M.; Geall, A.; Hermanson, G.; Kaslow, D.; Evans, T., A DNA-Based Vaccine for the Prevention of Human Cytomegalovirus-Associated Diseases. *Hum. Vaccines* **2005,** *1* (1), 16-23.

23. Steininger, C., Clinical Relevance of Cytomegalovirus Infection in Patients with Disorders of the Immune System. *Clin. Microbiol. Infect* **2007,** *13* (10), 953-963.

24. Cannon, M. J., Congenital Cytomegalovirus (CMV) Epidemiology and Awareness. *J. Clin. Virol* **2009,** *46*, S6-S10.

25. Williams, E. J.; Gray, J.; Luck, S.; Atkinson, C.; Embleton, N. D.; Kadambari, S.; Davis, A.; Griffiths, P.; Sharland, M.; Berrington, J. E.; Clark, J. E., First Estimates of the Potential Cost and Cost Saving of Protecting Childhood Hearing from Damage Caused by Congenital CMV Infection. *Arch. Dis. Child* **2015,** *100* (6), F501-F506.

26. Pires, F.; Silva, H.; Dominguez-Renedo, O.; Alonso-Lomillo, M. A.; Arcos-Martinez, M. J.; Dias-Cabral, A. C., Disposable Immunosensor for Human Cytomegalovirus Glycoprotein B Detection. Talanta **2015**, 136, 42-46.

27. Susmel, S.; O'Sullivan, C. K.; Guilbault, G. G., Human Cytomegalovirus Detection by a Quartz Crystal Microbalance Immunosensor. Enzyme and Microbial Technology **2000**, 27 (9), 639-645.

28. Dick, J. E.; Hilterbrand, A. T.; Boika, A.; Upton, J. W.; Bard, A. J., Electrochemical Detection of a Single Cytomegalovirus at an Ultramicroelectrode and its Antibody Anchoring. Proceedings of the National Academy of Sciences of the United States of America **2015**, 112 (17), 5303-5308.

29. Wang, R.; Wang, Y.; Lassiter, K.; Li, Y.; Hargis, B.; Tung, S.; Berghman, L.; Bottje, W., Interdigitated Array Microelectrode Based Impedance Immunosensor for Detection of Avian Influenza Virus H5N1. Talanta **2009**, 79 (2), 159-164.

30. Kang, J.; Rowntree, P. A., Gold Film Surface Preparation for Self-Assembled Monolayer Studies. Langmuir **2007**, 23 (2), 509-516.

31. Van Schaftinghen, T.; Le Pen, C.; Terryn, H.; Horzenberger, F., Investigation of the Barrier Properties of Silanes on Cold Rolled Steel. Electrochim. Acta **2004**, 49 (17-18), 2997-3004.

32. Lai, W.-A.; Lin, C.-H.; Yang, Y.-S.; Lu, M. S. C., Ultrasensitive and Label-Free Detection of Pathogenic Avian Influenza DNA by Using CMOS Impedimetric Sensors. Biosens. Bioelectron **2012**, 35 (1), 456-460.

33. Daniels, J. S.; Pourmand, N., Label-Free Impedance Biosensors: Opportunities and Challenges. Electroanalysis **2007**, 19 (12), 1239-1257.

34. Tarat, A.; Majithia, R.; Brown, R. A.; Penny, M. W.; Meissner, K. E.; Maffeis, T. G. G.; IEEE, Nanocrystalline ZnO Obtained from Pyrolytic Decomposition of Layered Basic Zinc Acetate: Comparison Between Conventional and Microwave Oven Growth. **2012** 12th IEEE Conference on Nanotechnology (IEEE-Nano) 2012.

35. Wahid, K. A.; Lee, W. Y.; Lee, H. W.; Teh, A. S.; Bien, D. C. S.; Abd Azid, I., Effect of Seed Annealing Temperature and Growth Duration on Hydrothermal ZnO Nanorod Structures and their Electrical Characteristics. Appl. Surf. Sci **2013**, 283, 629-635.

36. Zhou, J.; Zhao, F.; Wang, Y.; Zhang, Y.; Yang, L., Size-Controlled Synthesis of ZnO Nanoparticles and their Photoluminescence Properties. J. Lumin 2007, 122, 195-197.

37. Khoshhesab, Z. M.; Sarfaraz, M.; Asadabad, M. A., Preparation of ZnO Nanostructures by Chemical Precipitation Method. Synth. React. Inorg., Met.Org., Nano-Met. Chem **2011**, 41 (7), 814-819.

38. Katti, K. V., Synthesis and Reactivity in Inorganic, Metal-Organic and Nano-Metal Chemistry. Synth. React. Inorg., Met.Org., Nano-Met. Chem **2005**, 35 (1), 1-2.

39. Baruah, S.; Dutta, J., Effect of Seeded Substrates on Hydrothermally Grown ZnO Nanorods. , J. Sol-Gel Sci. Technol **2009**, 50 (3), 456-464.

40. Deegan, R. D.; Bakajin, O.; Dupont, T. F.; Huber, G.; Nagel, S. R.; Witten, T. A., Capillary Flow as the Cause of Ring Stains from Dried Liquid Drops. Nature **1997**, 389 (6653), 827-829.

Insert Table of Contents Graphic and Synopsis Here